**ORIGINAL ARTICLE**

CrossMark

# Characterization and prediction of chip formation dynamics in machining austenitic stainless steel through supply of a high-pressure coolant

Y. Seid Ahmed[1] · J. M. Paiva[1,2] · S. C. Veldhuis[1]

**Abstract**
Use of a high-pressure coolant supply (HPC) can lead to a considerable improvement in machining performance and process stability during the cutting of difficult materials such as stainless steels. Due to the high pressure of the coolant jet, a hydraulic wedge was formed at the tool–chip interface and thus reduced tool–chip contact length and friction behavior. Moreover, the cutting stability can be enhanced as a result of efficient chip breakability. The goal of this work is to evaluate how chip morphology is influenced by three thin jets of pressurized coolant directed into the tool–chip interface during machining of AISI 304 austenitic stainless steel and compare the resulting performance of the tool with dry and conventional coolant conditions. Furthermore, this research evaluates the influence of tool wear on the chip forming mechanism during the turning process. An analysis of the chip generated under machining emphasizes the hypothesis that variations in the cutting tool wear directly affect the chip shape and type of chip segmentation. Finally, a theoretical model was developed to predict the chip upcurl radius under HPC machining. This model is based on shear plane and structural mechanical theories which evaluate plastic strain and the bending moments along the length of the curled chip. The chip upcurl radius values from the developed theoretical model were found to be in good agreement with those measured in the machining tests.

**Abbreviations**

| | | | |
|---|---|---|---|
| HPC | High-pressure coolant | $\mu$ | Coefficient of friction |
| $f$ | Feed rate | $R_n$ | Natural chip upcurl radius |
| $r$ | Chip thickness ratio | $R_i$ | Initial chip upcurl radius |
| $t_c$ | Chip thickness | $R_f$ | Final chip upcurl radius |
| $t$ | Undeformed chip thickness | $L_c$ | Tool–chip contact length |
| | | $VB_B$ | Average flank wear |
| | | ASB | Adiabatic shear band |
| | | $h_1, h_2$ | Maximum and minimum chip thickness, respectively |
| | | $w$ | Distance between chip segments |
| | | $G_s$ | Degree of chip segmentation |
| | | $\varepsilon$ | Plastic strain |
| | | $\varepsilon_{fr}$ | Fracture strain |
| | | $\varepsilon_{chip}$ | Chip strain |
| | | $\varepsilon_{up}$ | Chip upcurl strain |
| | | $\phi$ | Shear angle |
| | | $\gamma$ | Rake angle |
| | | $\varepsilon x, \varepsilon y, \varepsilon z$ | Normal strain in X, Y, and Z directions, respectively |
| | | $\gamma_{xy}, \gamma_{yz}, \gamma_{xz}$ | Shear strain in X, Y, and Z directions, respectively |

✉ Y. Seid Ahmed
Seidahmy@mcmaster.ca

J. M. Paiva
paivajj@mcmaster.ca

S. C. Veldhuis
veldhu@mcmaster.ca

1 McMaster Manufacturing Research Institute (MMRI), Department of Mechanical Engineering, McMaster University, 1280 Main Street West, Hamilton, ON L8S4L7, Canada

2 Department of Mechanical and Materials Science, Catholic University of Santa Catarina, Rua Visconde de Taunay, 427-Centro, Joinville, SC 89203-005, Brazil

| $\varepsilon_a, \varepsilon_b$ | Normal strain components in the ab coordinate system |
|---|---|
| $\gamma_{ab}$ | Shear strain in the ab coordinate system |
| $\psi$ | Rotation angle around the third axis |
| $\theta$ | Rotation angle in the XYZ system |
| $\delta$ | Spiral angle |
| $I_1, I_2, I_3$ | Stress invariants |
| $R_1$ | HPC force |
| $R_2, R_3$ | Reaction forces acting on the chip body |
| $\omega_1, \omega_2$ | Angle between vertical line and $R_1$ and $R_2$, respectively |
| $\sigma$ | Angle between $R_3$ and horizontal line |
| $F_3, F_{n3}$ | HPC force components |
| $M$ | Bending moment |

# 1 Introduction

Machining of austenitic stainless steel is considered as a difficult-to cut material due to high strain hardening, high ductility, and low thermal conductivity. These properties promote high cutting temperature and continuous chips which can cause serious problems during machining [1]. In this context, the high-pressure coolant (HPC) is a modern technology that has significant potential to improve the process which satisfies the industry's demand [2]. The HPC system delivers sufficient cooling at the tool–workpiece interface and effective chip evacuation from the cutting area [3]. The adequate penetration of HPC into the tool–chip interface reduces the machining temperature and consequently the seizure effect, minimizing the friction at the cutting zone [4]. In addition, the coolant jet is able to create a coolant wedge under high pressure, which forms between the cutting tool and the chip to bend upwards, thus enhancing the chip formation process and chip control [5].

Several studies have concluded that this machining technique improves chip characteristics compared to the conventional coolant. Furthermore, HPC can be used to break apart chips during machining [6]. Mazurkiewicz et al. [7] used a high-pressure water jet in their investigation to study its effect on the machining performance. The authors found that the chip thickness and chip compression ratio were decreased, consequently improving machining performance. Kaminski and Alvelid [6] investigated the impact of HPC and the conventional coolant system on chip shape and friction behavior during the turning process. The authors showed that conventional coolants are ineffective due to their low pressure at the interface, which contributes to extreme friction conditions at the cutting zone. Moreover, Courbon et al. [8] and Palanisamy et al. [9] compared the effect of both conventional coolant and HPC on tribological performance. Their investigation showed that HPC was able to reduce the chip thickness and increase

the shear angle compared to the larger chip thickness and smaller shear angle under a conventional coolant.

Despite a high number of HPC application studies, few papers discuss the advantages of HPC for chip control during stainless steel machining, and there is no study on the prediction of chip breakability under HPC. Chip control during machining of stainless steel is gaining wide attention due to its vital role in increasing machining productivity [10]. Due to the lack of theoretical methods which can quantify HPC chip breakability, it becomes difficult to control chip breakability with a good level of accuracy [11, 12]. Bai [13] and Okushima et al. [14] reported that the undeformed chip thickness and the chip upcurl radius affect the chip breakability. It was concluded that the chip fracture increased either in reverse relation to the chip upcurl radius or with an increase in the undeformed chip thickness.

Considering the gaps in the literature review, this research aims to investigate the chip forming mechanism and chip breakability of AISI 304 stainless steel with a supply of HPC directed to the tool–chip interface. The experiments were conducted at different cooling conditions: dry condition, conventional coolant supply, and two pressures of HPC. The chip formation mechanism, based on the microscopic images of the chip's form, is evaluated in terms of chip characteristics, segmentation, and free surface. The second part of this study includes a three-dimensional (3D) theoretical model of chip curling during metal cutting, which evaluates the effect of HPC supply on chip geometry. Finally, the experimental results are used to validate the theoretical model.

# 2 Experimental procedure

## 2.1 High-pressure coolant and machining system

Experimental trials were performed on a CNC lathe model using a Nakamura-Tome Sc-450. The cutting fluid used in the cutting processes was a semi-synthetic coolant at a concentration of 6% that was employed by a conventional coolant system at a pressure of 0.7 bar and flow rate of 2.7 L min$^{-1}$. Uncoated cemented carbide tools (WC 6%Co) were used for the experiments, and the ISO code for the cutting inserts is WNMG 06 04 08-SM 1105. These inserts are recommended by the manufacturer [15] and Koyee et al. [16] for machining stainless steels. The cutting tool holder has ISO specification PWLNR 16-4DHP, supplied by Sandvik. This tool holder is specially designed for use with HPC. The tool holder has three cooling nozzles (1.5 mm in diameter) to deliver HPC very close to the cutting zone, as shown in Fig. 1. The nozzles make an 18° angle with the rake face, and the distance between the nozzles and the tooltip is around 25 mm which helps reach the proximity of the tool–chip contact zone and eliminate the possible interference between the nozzle and the removed

**Fig. 1** **a** The HPC tool holder. **b** Direction of HPC on the cutting tool. **c** Drawing of tool holder showing the geometry of nozzles [46]
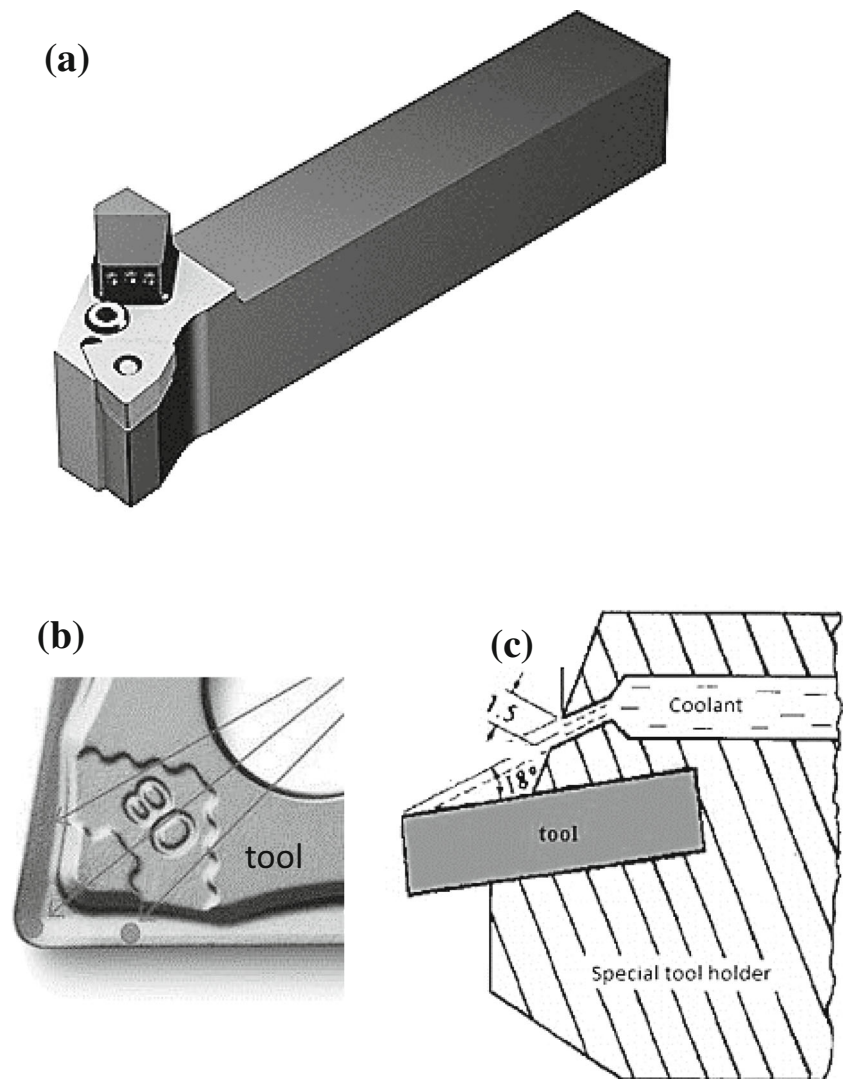


chips. Figure 2 presents the machining system including an external high-pressure pump and workpiece/cutting tool setup system. The pump is able to provide a coolant with pressures from 0.1 to 70 bar and flow rate of 90 L min$^{-1}$. Four trials were performed: (a) using HPC (with 35 and 70 bar), (b) using a conventional coolant system, and (c) dry condition. The choice of 35 and 70 bar is based on the output pressure limit of the HPC supply system.

## 2.2 Workpiece material characterization

The workpiece was an AISI 304 austenitic stainless steel round bar with a length of 500 mm and a diameter of 120 mm. Table 1 shows the mechanical and chemical compositions of the AISI 304 as provided by the material manufacturer. A sample of the AISI 304 was cut from the round bar and then cold mounted and polished. A glyceregia solution (20 mL $HNO_3$ + 1 mL glycerol + 20 mL hydrochloric acid

(HCl)) served as etching fluid to show the microstructure, and the microstructure observation was conducted using a Nikon ECLIPSE IV 100 microscope, equipped with a UC30 camera. On Fig. 3, it is possible to see the microstructure of the material.

## 2.3 Cutting tests

According to the recommendations of the manufacturer, the cutting conditions were formed with a feed rate of 0.1 mm/rev, depth of cut of 0.5 mm, and cutting speed of 60 m/min. These cutting conditions are within the recommended range by the manufacturer [15], and they are commonly applied in the industry for machining austenitic stainless steel. During the experiments, average tool flank wear ($VB_B$) was measured with an optical microscope (KEYENCE VHX-5000). Each test was repeated at least three times. The tool failure criteria can be estimated by a maximum $VB_B$ of 0.3 mm [17]. Moreover,
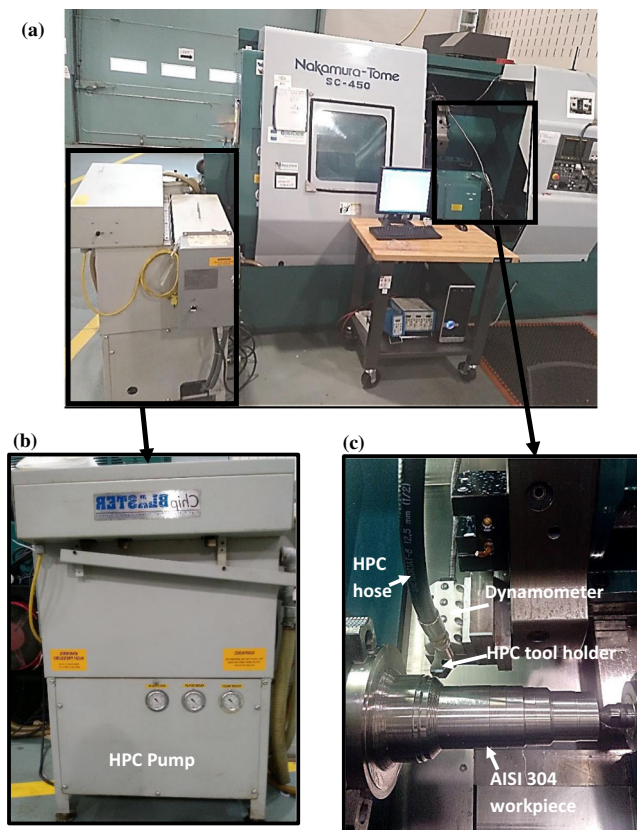
Fig. 2 The machining process used in the experimental work with the high-pressure coolant supply
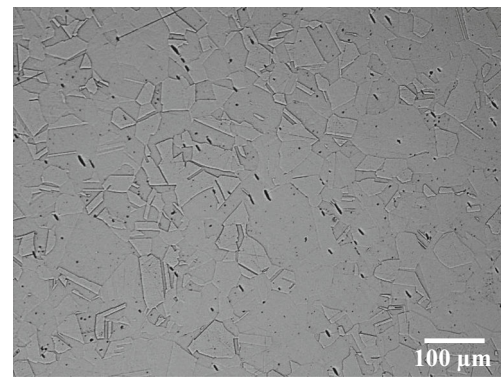


Fig. 3 The microstructure of AISI 304 with an austenitic structure

positioned at a 70° tilt angle, and working distances ranged between 8 and 12 mm. The chips cross sections were phase-mapped using Tango-Maps software and processed using Channel 5 HKL.

Besides, the average chip thickness and chip upcurl radius, obtained with different cooling conditions and flank wear values, were measured. Next, the chip thickness ratio, the friction coefficient, and the shear angle at the tool–chip interface were calculated according to Shaw [18]. The chip free surface and chip undersurface under the same conditions mentioned above were also analyzed using SEM to understand the chip forming mechanism and the friction behavior at the tool–chip interface. The average surface roughness of the chip undersurface was evaluated using white light interferometry (Alicona Infinite Focus) [19].

the cutting tools were investigated with a scanning electron microscope (SEM) facility (VEGA3 TESCAN).

The chips obtained after machining with the new and worn tools ($VB_B$ = 0.1, 0.2, and 0.3 mm) at different cooling conditions (dry, conventional coolant, HPC (35 and 70 bar)) were mounted with epoxy so that the chip cross section could be seen. After appropriate preparation, the cross sections were observed with SEM and electron backscatter diffraction (EBSD) to analyze chip morphology and to conduct an adiabatic study of the shear bands and crack formation. No etching treatment was used on the samples for EBSD analysis. The SEM images were acquired under high current, 10 mm working distance, and 60 μm aperture operating at 20-kV accelerating voltage. EBSD scans were performed in a JEOL-6610LV high-resolution scanning electron microscope, operating at 20 kV and 60-μm aperture size. A CCD detector was used at a 176-mm insertion distance. The sample was

## 3 Experimental results and discussion

### 3.1 Chip morphology: effect of high-pressure coolant

#### 3.1.1 Chip form and segmentation

The chips produced throughout the turning experiments were collected to investigate their morphology (shapes, structures, geometry) and to provide an in-depth study of chip formation under HPC use. Figure 4 gives an overview of the resultant chip types depending on the coolant conditions. It can be shown that the turning of stainless steel under a dry and conventional coolant produced continuous chips, whereas HPC produced smaller segmented chips. HPC conditions help to break up chips,

Table 1 Chemical composition and mechanical properties of AISI 304 stainless steel

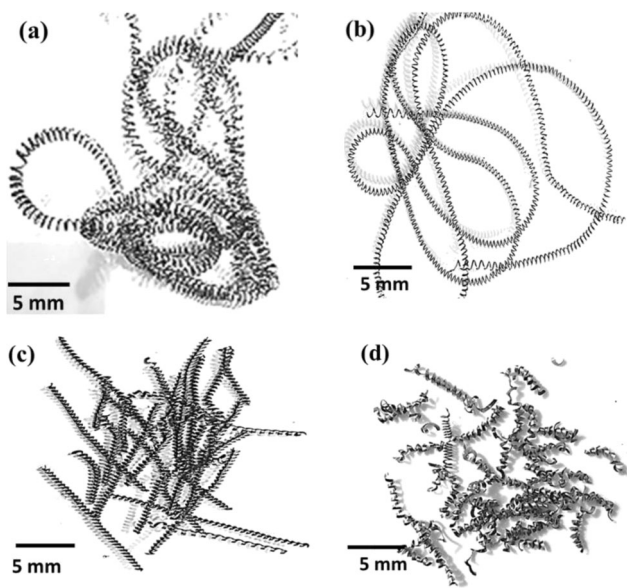| | | | Chemical composition (%) | | | | |
|---|---|---|---|---|---|---|---|
| C | Si | Mn | P | S | Cr | Ni | N |
| 0.08 | 0.75 | 2.0 | 0.045 | 0.03 | 20.0 | 0.50 | 0.10 |
| Proof strength (0.2% yield, MPa) | Tensile strength (MPa) | Elongation (%) | Modulus of elasticity (GPa) | | Shear modulus (GPa) | Hardness HRC | |
| 215 | 505 | 70 | 200 | | 86 | 70 | |

**Fig. 4** Chip formation at different cutting conditions: **a** dry, **b** conventional coolant, **c** HPC (35 bar), and HPC (70 bar)

producing shorter segmented chips [20]. In contrast, the dry and conventional coolant did not show the distinct effect on chip formation. Under the dry and conventional coolant, chip fracture occurs because of the force generated by an obstruction-type chip breaker [10, 13, 21–23]. However, enhanced chip breaking occurring under HPC is a consequence of the high force created by the HPC system [24]. The 35- and 70-bar coolant pressures are large enough to break the chip, before it comes in contact with an obstruction [21].

Furthermore, the HPC supply can remove the chips beyond the deformation zone, reducing the tool–chip contact area and improving the friction conditions at the interface [22] which helps to enhance chip undersurface morphology as well as

chip fragmentation [25]. To confirm this behavior, the chip undersurface morphology showing the chip flow and the surface roughness is presented in Fig. 5. A substantial difference in chip undersurface morphology is evident: HPC application results in smoother chip undersurface (Ra = 0.54 μm) compared to dry cutting (Ra = 0.89 μm), where a clear stick–slip phenomenon is present. This means that the application of HPC improves tribological conditions as a consequence of the smaller contact area [26].

To investigate the role of the HPC system on chip form, the chip cross sections were analyzed using SEM and EBSD analysis, and their data presented in Fig. 6. As shown, continuous chips obtained with dry and conventional coolants were compared to serrated chips with a supply of HPC, where periodic adiabatic shear bands (ASBs) and cracks were observed. Adiabatic shear bands result from thermo-mechanical instability, which increases shear deformations in small areas [27]. This highly localized strain leads to a considerable increase in temperature, and in turn, ASBs [23]. It is commonly known that materials with low strain rates do not show ASBs because heat expansion creates a uniform temperature in the workpiece [28]. Under HPC, the high positive bending moment contributes to the growth of ASBs' frequency, which leads to an increase of the plastic strain in the formed chip [29]. Once the chip strain exceeds the chip breaking strain, cracks develop on the ASBs that separate the adjacent segments [30]. As indicated, under HPC conditions in Fig. 6e–h, the degree of serration in the chip as well as the crack size (the crack depth is around 20 μm) depend on the strength of the shearing action caused by HPC. Also, although no segmentation can be seen in the dry and conventional coolant (Fig. 6a, c), very well-defined segmented chips are generated under HPC conditions (Fig. 6e, g). In order to examine the shear band differences in more details, EBSD analysis was used to investigate the highly deformed shear

**Fig. 5** Chip breaking under various cooling conditions, associated with chip undersurface obtained with **a** dry, **b** conventional coolant, **c** HPC of 35 bar, and **d** HPC of 70 bar
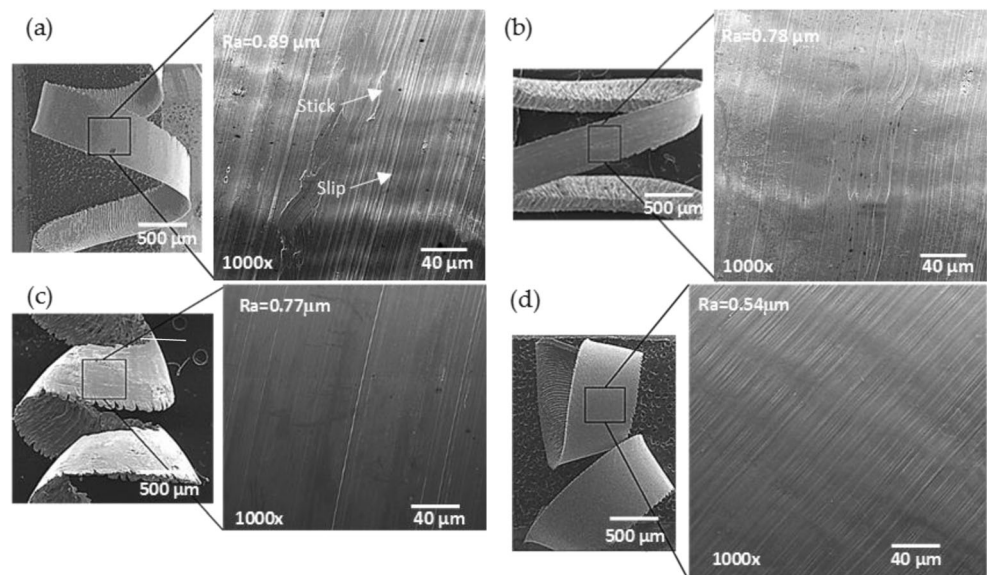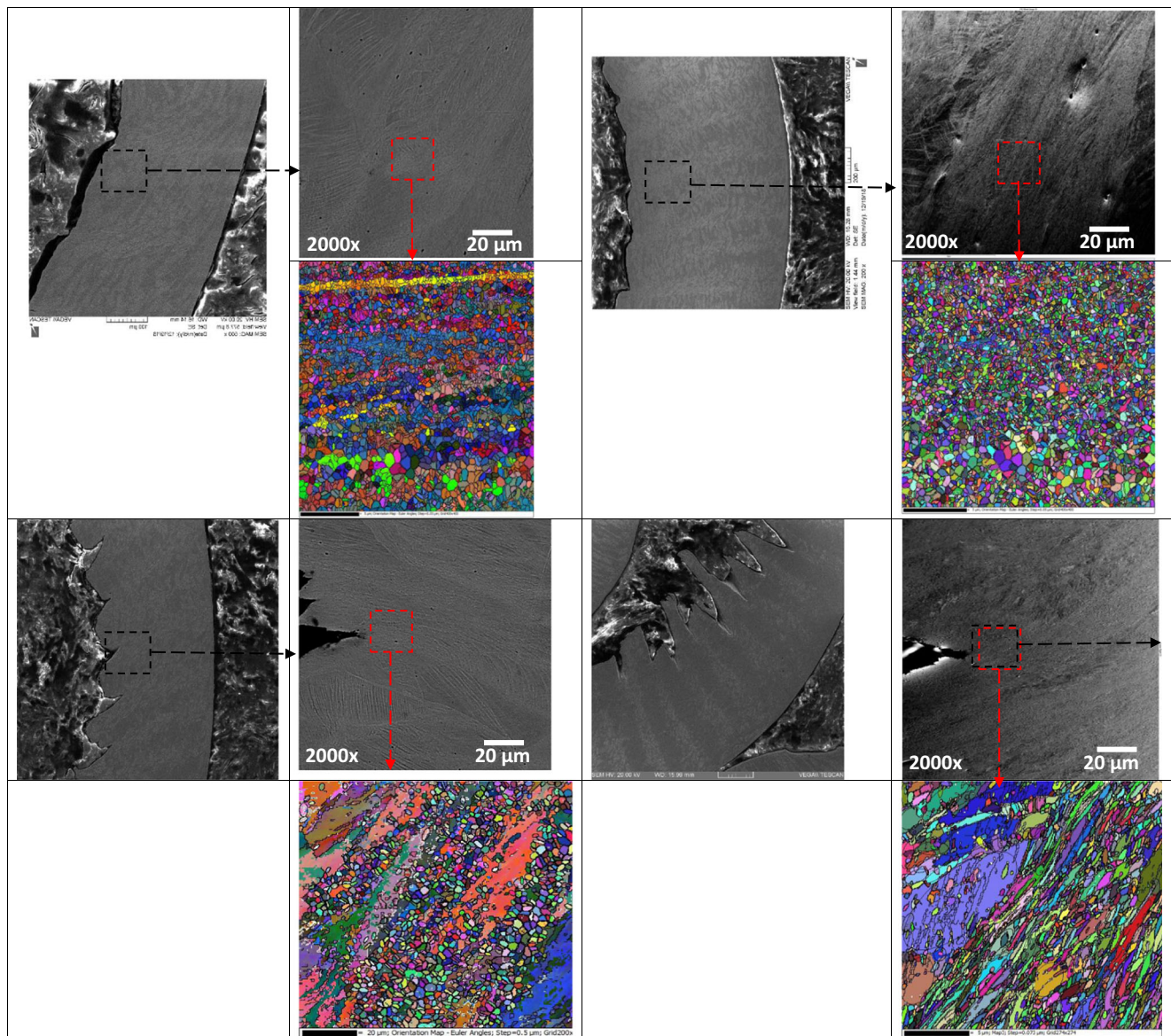
**Fig. 6** SEM and BSE images of chip cross sections associated with orientation maps obtained under different cutting conditions: **a**, **b** dry, **c**, **d** conventional coolant, **e**, **f** HPC of 35 bar, and **g**, **h** HPC of 70 bar

regions within each chip. The resulting orientation maps of the regions taken from the chips in Fig. 6e, c, e, g are shown in Fig. 6b, d, f, h, respectively. As shown, it can be observed that the grains are more elongated in case of HPC conditions which conforms to the severe plastic deformation caused by HPC application. Here, the shear bands formed by the dry and conventional coolant have very equiaxed grains (~1 μm) compared with a mixture of equiaxed grains (~3 μm) and very elongated grains in case of HPC conditions.

In addition, the chip thickness was also evaluated. The data that characterize chip serration are presented in Fig. 7a. In this figure, $h_1$ and $h_2$ represent, respectively, the highest and lowest chip thickness, and $w$ represents the distance between segments. The values of $h_1$ and $h_2$ at distinct cooling conditions

were measured, and the results are presented in Fig. 7b. The difference between $h_1$ and $h_2$ is observed, and the values decrease under the supply of HPC. This also agrees with the previous conclusion that the HPC can enhance chip segmentation during the machining process. On the other hand, there is no noticeable difference between the values of $h_1$ and $h_2$ in case of dry and conventional coolant; these results confirm the previous conclusion that no segmentation can be observed under the use of dry and conventional coolant.

Furthermore, the distance between segments ($w$) was measured and is presented in Fig. 7c–f. The distance between segments is 0.15–0.155 mm and 0.140–0.145 mm for 35 and 70 bar, respectively (Fig. 7e, f) compared with 0.17–0.175 mm and 0.160–0.165 mm for dry condition and

**Fig. 7** **a** Parameters of chip serration. **b** The values of maximum and minimum chip thickness for different cooling conditions. **c**–**f** Micrographs of serrated chip cross sections showing the average distance between segments at **c** dry, **d** conventional coolant, **e** HPC of 35 bar, and **f** HPC of 70 bar
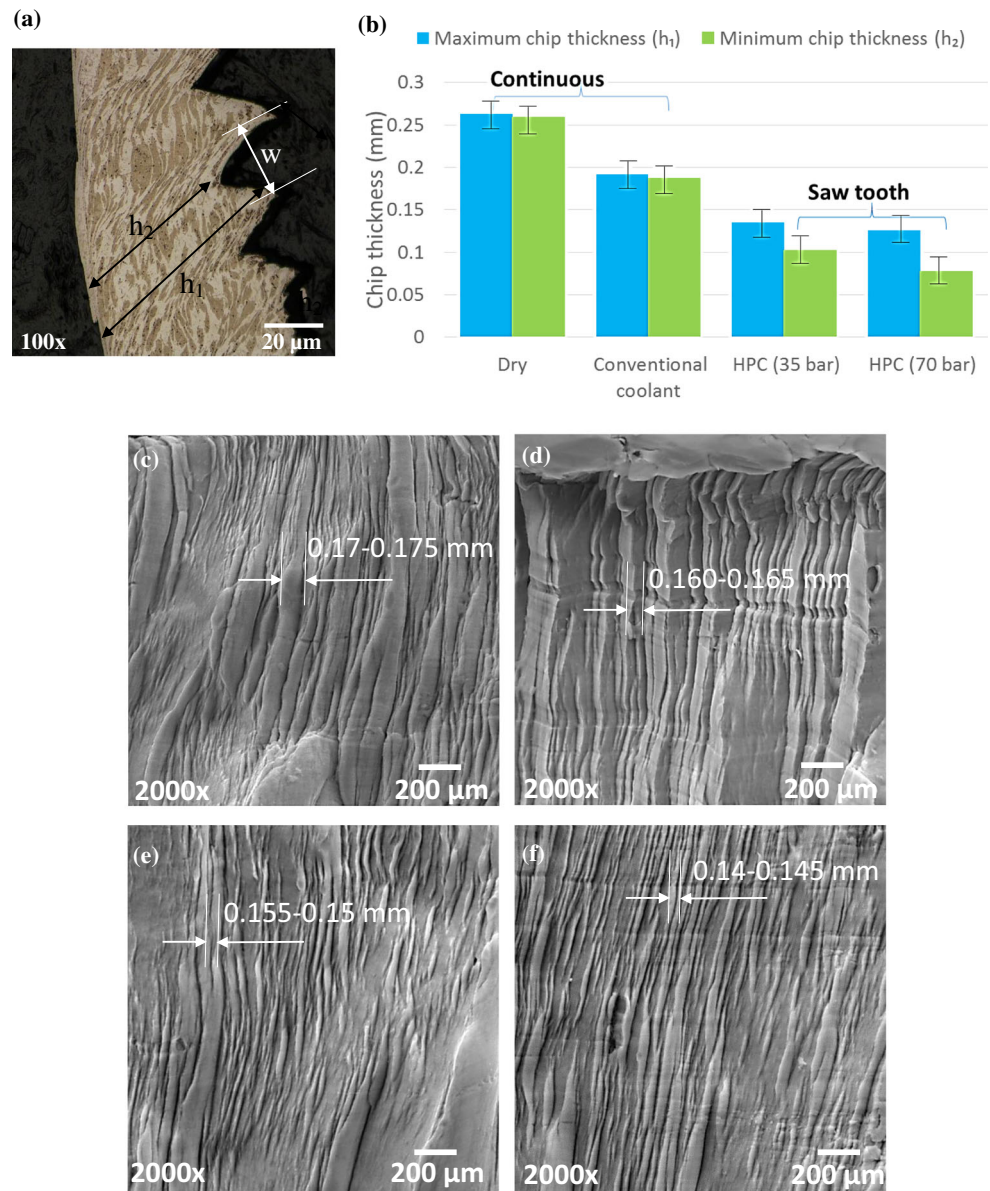


conventional coolant, respectively, as shown in Fig. 7c, d. The distance between segments was found to decrease under HPC, which promotes greater shear formation during the turning process of stainless steel [25].

### 3.1.2 Chip characteristics

The thickness of the chips ($t_c$) and the tool–chip contact length ($L_c$) were measured according to the different cutting conditions proposed in this work. An example of measured tool–chip contact length is shown in Fig. 8. From the chip characteristic results illustrated in Table 2, it is possible to see that there is an apparent difference in shear angle and coefficient of friction values for both the dry coolant and HPC. In this case, the chips obtained by HPC produced larger shear angles and a

lower coefficient of friction. This phenomenon is a response to the effect of HPC jets directed onto the cutting zone. As a consequence of better fluid access into the cutting zone, the tool–chip contact length is improved, resulting in lower chip thickness compared to dry and conventional conditions. Therefore, machining of AISI 304 under an HPC system produces a short shear area, which leads to thinner chips [8–11, 31] and lower cutting forces and friction coefficient [32].

## 3.2 Chip morphology: effect of tool wear

### 3.2.1 Chip segmentation frequency

The degree of chip deformation was obtained for five different continuous chip segments, and the mean value was used.
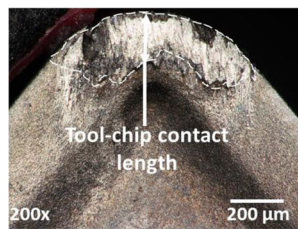
**Fig. 8** Tool-chip contact length

Based on the measured parameters shown in Fig. 7a, the degrees of chip segmentation can be calculated from Eq. 1.

$$G_s = \frac{h_1 - h_2}{h_2} \tag{1}$$

The graph in Fig. 9 presents the relation between the degree of tool wear and chip segmentation. The measurements show that during the initial phase (new cutting tool insert), a continuous chip is generated in dry condition. Once a particular tool wear degree is reached ($F_w = 0.2$ mm), the chip forming mechanism switches to produce a saw–tooth chip form. On the other hand, no clear variation was found in the degree of segmentation at different flank wears under HPC conditions, which indicates that flank wear did not affect the chip segmentation when HPC is used.

Also, the variations in segmented chip features under increasing flank wear for dry conditions and HPC are summarized in Table 3. As in the dry condition, $h_1$ and $h_2$ significantly increased along with the flank wear: these results confirm the previous conclusion that the chip's structure is changed from continuous to saw-tooth form. In contrast, no significant difference in $h_1$ and $h_2$ values was found upon an increase in flank wear in the case of HPC due to high plastic deformation generated by HPC during the cutting process. Furthermore, a slight increase in the chip width was observed around the flank wear in both conditions: dry and HPC. This condition is related to high wear and results in an unsharpened cutting tool, which consequently leads to a rough chip edge formation.

As discussed, the transformation from continuous chip to saw-tooth chip under dry and conventional coolant is accompanied by an increase in flank wear. Investigation of the chips' free surface obtained under dry condition reveals two distinct structures, the most frequently observed of which is the lamellar structure (Fig. 10a). A difference in the chips' free surface geometry was investigated just prior to the formation of chip

segments caused by an increase in flank wear. These new geometries, shown in Fig. 10b, have been termed as folds. Further increase in flank wear leads to more deformation, which in turn can enhance the formation of saw-tooth chips (Fig. 10c).

### 3.2.2 Free surface of chips

Figure 11a, b shows the free surface of typical chips obtained with new and worn tools under dry and HPC conditions. A lamellar structure is evident on the underside of the chips obtained under dry conditions and HPC (Fig. 11b, g). At high magnification, it is observed that each segment of the free surface has slipping and undeformed surfaces (Fig. 10c, h). With the new tool, the slipping surface features a high number of dimples (Fig. 11c, h), as a result of high plastic deformation during chip segmentation. As shown, the incidence of dimples in case of HPC is greater compared to the dry condition, which confirms that HPC is capable of increasing the plastic deformation during cutting and consequently, the fracture mechanism. On the other side, it can be seen that there are sliding lines on the undeformed surface, as described in Fig. 11c, h, which were produced by high friction between the cutting tool and the workpiece (the frequency of sliding lines is less in HPC, since the tool–chip contact length is lower (Table 3)).

When the cutting tool reaches its maximum wear ($VB_B = 0.3$ mm) under the dry condition, the frequency of undeformed surfaces is greater than that of the new tool because the chips are transformed from continuous into segmented types, as described in Fig. 9. Also, the deformation on the slipping surface shows an obvious viscous behavior (Fig. 11e), which indicates that the cutting temperature is much higher at tool failure compared to that of a fresh tool. In contrast, at the end of tool life with HPC, no viscous behavior is observed (Fig. 11j), which indicates that the HPC is capable of significantly decreasing the cutting temperature even at a greater flank wear.

## 4 Understanding the chip breaking process

During the machining operation, the penetration of the coolant at the tool–chip interface affects the chip formation and its

**Table 2** Cutting characteristics at various cooling conditions

| Cooling condition | Chip thickness (mm) | Chip-tool contact length (mm) | Chip thickness ratio | Shear angle (°) | Theoretical coefficient of friction |
|---|---|---|---|---|---|
| Dry | 0.263 | 0.33 | 0.38 | 20.8 | 0.56 |
| Conventional coolant | 0.192 | 0.27 | 0.52 | 27.4 | 0.416 |
| HPC (35 bar) | 0.135 | 0.22 | 0.74 | 36.2 | 0.234 |
| HPC (70 bar) | 0.126 | 0.21 | 0.79 | 38.3 | 0.206 |

**Fig. 9** Correlation between tool-wear degree and chip-segmentation degree associated with SEM of chips
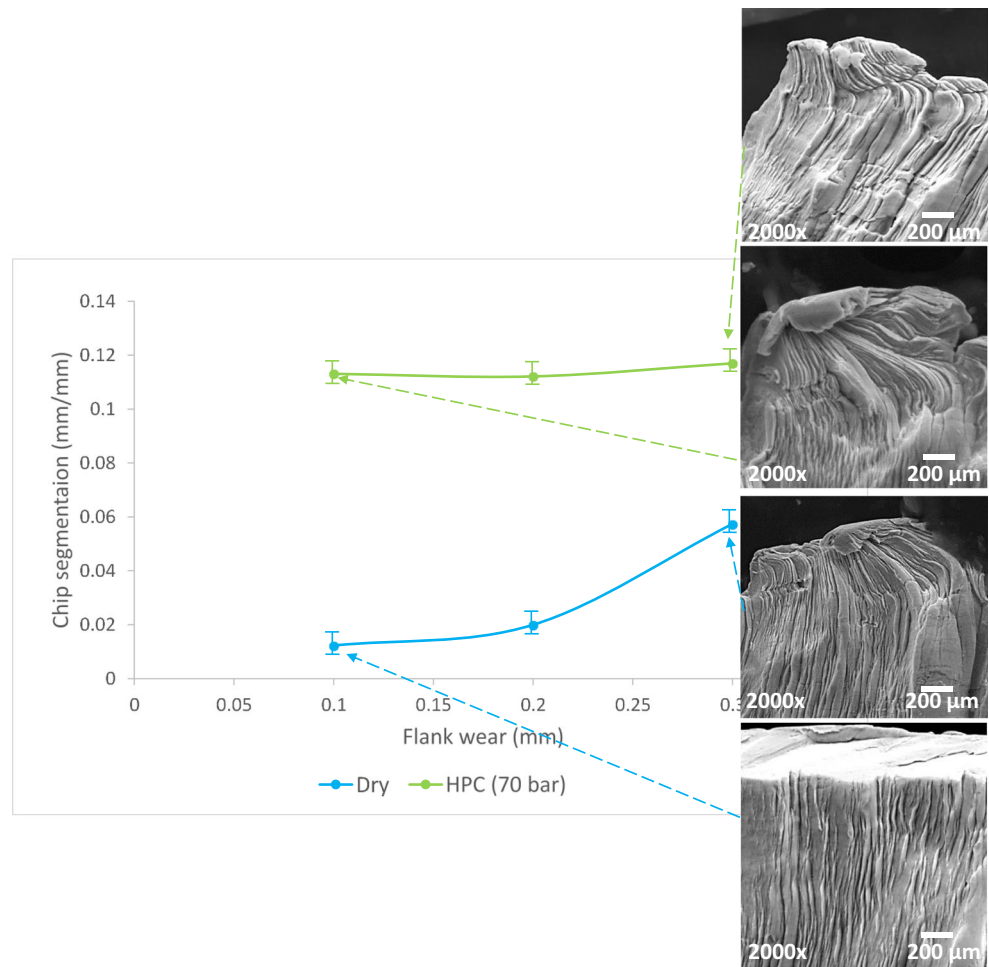


removal from the cutting area [33]. Since machining involves a great deal of chip formation processes, their breaking mechanisms have been studied for many years [5, 7, 17, 18]. The mechanisms of chip breaking are found to be affected by different parameters, such as machining conditions, workpiece material, tool insert geometry, cutting fluid, and pressure level [6, 9]. In this section, the theory of chip breaking will be discussed in general and then the influence of HPC on chip breakability will be investigated. Following the chip breaking theory, the chip upcurl radius will be measured at

**Table 3** Chip characteristics at various cooling conditions and various flank wear values

| Cooling condition | Flank wear (mm) | Maximum chip thickness (mm) | Minimum chip thickness (mm) | Distance between segments (mm) |
|---|---|---|---|---|
| Dry | 0.1 | 0.251 | 0.248 | 0.175 |
| | 0.2 | 0.255 | 0.253 | 0.185 |
| | 0.3 | 0.259 | 0.251 | 0.198 |
| Conventional coolant | 0.1 | 0.185 | 0.183 | 0.165 |
| | 0.2 | 0.189 | 0.185 | 0.173 |
| | 0.3 | 0.191 | 0.189 | 0.185 |
| HPC (35 bar) | 0.1 | 0.137 | 0.122 | 0.160 |
| | 0.2 | 0.137 | 0.122 | 0.168 |
| | 0.3 | 0.138 | 0.122 | 0.172 |
| HPC (70 bar) | 0.1 | 0.128 | 0.115 | 0.150 |
| | 0.2 | 0.129 | 0.117 | 0.163 |
| | 0.3 | 0.129 | 0.116 | 0.178 |
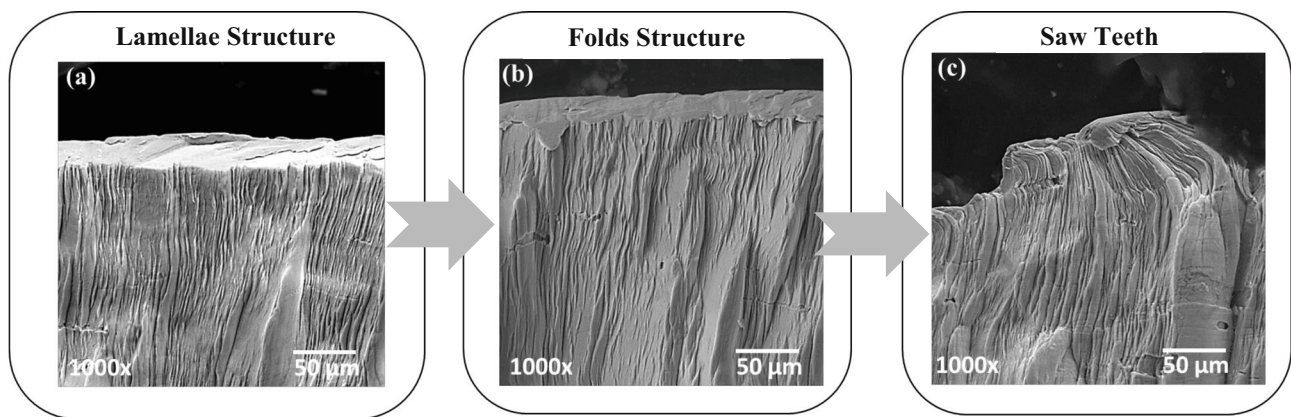
**Fig. 10** **a** Lamellae on the free surface of a continuous chip. **b** Folds formed on the free surface of a continuous chip produced under the same conditions as the chip in **a**. **c** Saw-tooth form chip under the same conditions as the chips in **a**, **b**

different cooling conditions to study the impact of different cooling conditions on the chip curling behavior.

## 4.1 Chip breaking theory

Chip curling mainly depends on the direction of chip flow [23]. The chip curl geometry is defined by three parameters, side curling, upcurling, and twisting [34] (Fig. 12a–c). The chip upcurl radius ($R_f$) has an important influence on chip breakability where the upcurl is dominant [11]. The chip breaking process occurs when strain on the chip body exceeds the maximum strain of chip material which is mainly the result of forces generated by HPC [36]. These contact forces will generate a moment leading up to chip fracture [35], and this is expressed as

$$\varepsilon_{\text{chip}} = \frac{t_c}{2}\left[\frac{1}{R_f} - \frac{1}{R_n}\right] \geq \varepsilon_{fr} \qquad (2)$$

where $t_c$ is the chip thickness, $R_n$ is the natural chip radius, and $\varepsilon_{fr}$ is the breaking strain.

Mathematical equations utilizing the above formula were characterized by Nakayama et al. [37]. The formulations of chip curl are qualitatively defined, and they have been used for many years to predict the chip breaking behavior. However, these equations miss the linkage between HPC and chip curling. Thus, understanding the role of HPC on the chip upcurl radius is necessary to predict chip breakability during machining.

To understand the relation between HPC and chip curling, Fig. 12d illustrates how HPC can affect the chip curling process. As shown, the mechanism of chip curling through the HPC system is a continuous process. After deformation occurs at the primary shear plane, the chip starts to grow and curl due to the high pressure of the HPC system [38]. Then, due to the high force of the HPC, the chip further grows until it reaches the limit of the chip material strain [5]. The most probable

point of breakage is where the HPC is at its maximum strength, forcing the chip away from the cutting tool [12]. In the meantime, a new chip is formed and the process repeats itself [39].

## 4.2 Chip upcurl radius measurement

The final chip upcurl radius was measured to quantify the above observations and relate them to the cutting conditions. The main part of this study focuses on the capability to employ chip upcurling as a method to verify the theoretical model of chip breaking in the machining operation.

After each test, the chips were collected and scanned using SEM to measure the chip upcurl radius. The variation of the chip radius with respect to the cooling conditions is shown in Fig. 13. It seems that the final chip upcurl radius depends on the coolant conditions. Firstly, under the dry and conventional coolant, the chips showed a large radius which corresponds to the shape of the chip space of the cutting tool [5]. The larger tool-chip contact length results in a greater tendency of material sticking on the cutting tool, restraining further chip movement [22]. In contrast, under HPC conditions, the chips become smaller, reducing chip length as well as the final chip upcurl radius [40].

## 5 Theoretical modeling of chip curling

In this section, a 3D theoretical model will be developed to predict the chip upcurl radius under HPC. To derive the model, the effect of plastic strain on chip free surfaces will be derived individually in Section 5.3. Next, the effect of HPC on the chip body will be investigated in Section 5.4. The model is based on the shear plane and structural mechanical theories involving plastic strain and bending moments along the length of the curled chip caused by HPC.
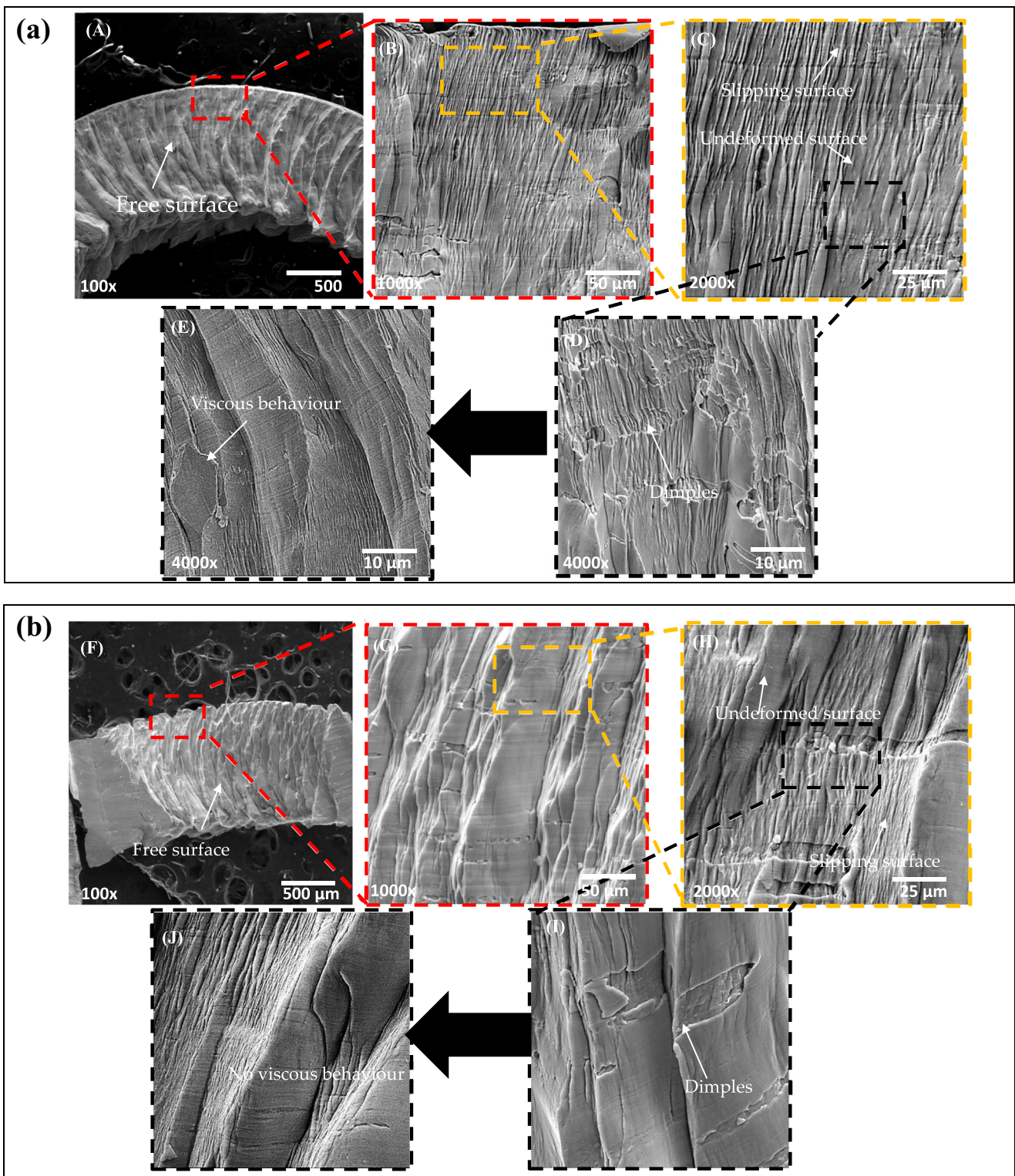
**Fig. 11** Chip morphology obtained in **a** dry and **b** HPC; (A–D) and (F–I) images of free chip surface, generated with new tool and (E–J) with worn tool

## 5.1 Theory

In the theoretical model, it is assumed that the cutting tool is rigid with the rake angle ($\gamma$) and the undeformed and formed chip thicknesses are denoted $t$ and $t_c$, respectively. Merchant [41] applied the shear plane theory (Fig. 14a) to derive an expression for the plastic strain as
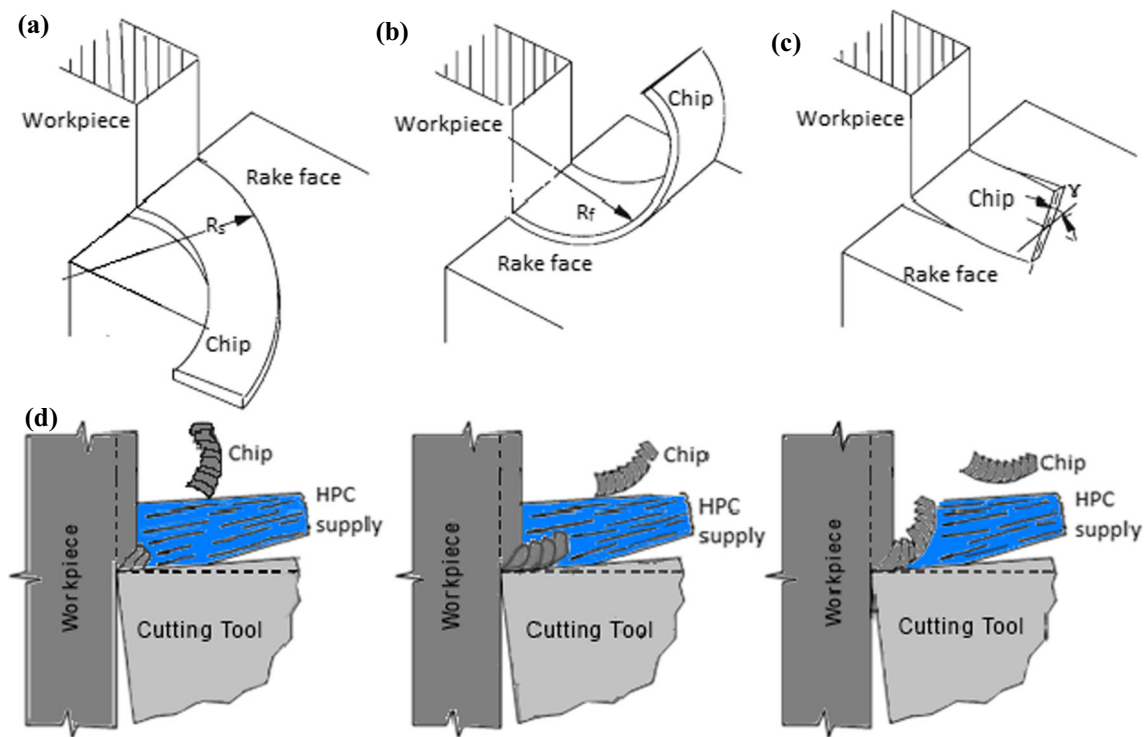
**Fig. 12** **a–c** Parameters of chip curl radius. **a** Chip upside radius. **b** Chip upcurl radius. **c** Twisting. [35]. **d** The formation of segmented chips under HPC supply [15]

$$\varepsilon = \frac{\cos\gamma}{\cos(\Phi - \gamma)\sin\Phi} \tag{3}$$

where $\Phi$ is the shear angle.

Astakhov and Shevets [42] modified Eq. 3 and used a von Mises yield criteria to derive the plastic strain on the chip free surface during 3D chip formation, and the derived equation is as follows:

$$\varepsilon = \frac{\sqrt{2}}{3}\left[\left(\varepsilon_x - \varepsilon_y\right)^2 + \left(\varepsilon_y - \varepsilon_z\right)^2 + \left(\varepsilon_z - \varepsilon_x\right)^2 + 6\left(\gamma_{xy}^2 + \gamma_{yz}^2 + \gamma_{zx}^2\right)\right]^{0.5} \tag{4}$$

where $\varepsilon_x$, $\varepsilon_y$, $\varepsilon_z$, $\gamma_{xy}$, $\gamma_{xz}$, and $\gamma_{yz}$ are the strain components of the strain tensor.

From literature, there are many authors who used the plastic chip strain as a method for predicting the chip breaking process. They showed that by decreasing the chip upcurl radius, the tendency of chip failure increases by enhancing the chip plastic strain [5, 7]. Nakamura [37] presented a relation of the plastic chip strain, which developed from the initial chip upcurl radius to the final chip upcurl radius (Eq. 2).

However, there are many researches in this field; the scarcity of the basic theory for 3D plastic flow and the study on the effect of HPC on chip breakability make it difficult to develop a 3D oblique cutting model. Here, the objective is to introduce these parameters to make the model simpler to develop. A 3D oblique process can be treated as a modification of a 2D orthogonal cutting process [43]. Therefore, the fracture mechanism of the 3D process can be described by the 2D bending of a curved beam [44]. The only difference here between Nakamura equation and Eq. 5 is that the used parameters should be replaced by their corresponding parameters, i.e.,

$$\varepsilon_{up} = \frac{t_c}{2R_f} \tag{5}$$

where $t_c$ is the maximum chip thickness, $R_f$ is the radius of chip fracture, and $\varepsilon_{up}$ is the chip strain.

However, few authors derived theoretical models that show the effect of plastic strain on chip curling. A clear understanding of the mechanism of chip breakability under HPC use is yet to be found. The bending moment and forces acting on the chip body through HPC play a key role in the chip curling and breaking process [38]. The chip's formation out of the cutting tool edge's meeting point with the workpiece is considered to be a plastic deformation process [45]. After this process occurs, the material of the chip shows obvious strain hardening. Thus, it is assumed that the chip generated after HPC has no further plastic deformation [38]. The chip is presumed to move with an angular speed as a static structure. By understanding how the forces and bending moments affect the chip body, the chip breakability will be investigated.

In summary, chip upcurling plays a vital role on chip breakability. The impact of HPC on chip upcurling

**Fig. 13** Chip upcurl radius under different cooling conditions: **a** dry, **b** conventional coolant, **c** HPC of 35 bar, and **d** HPC of 70 bar
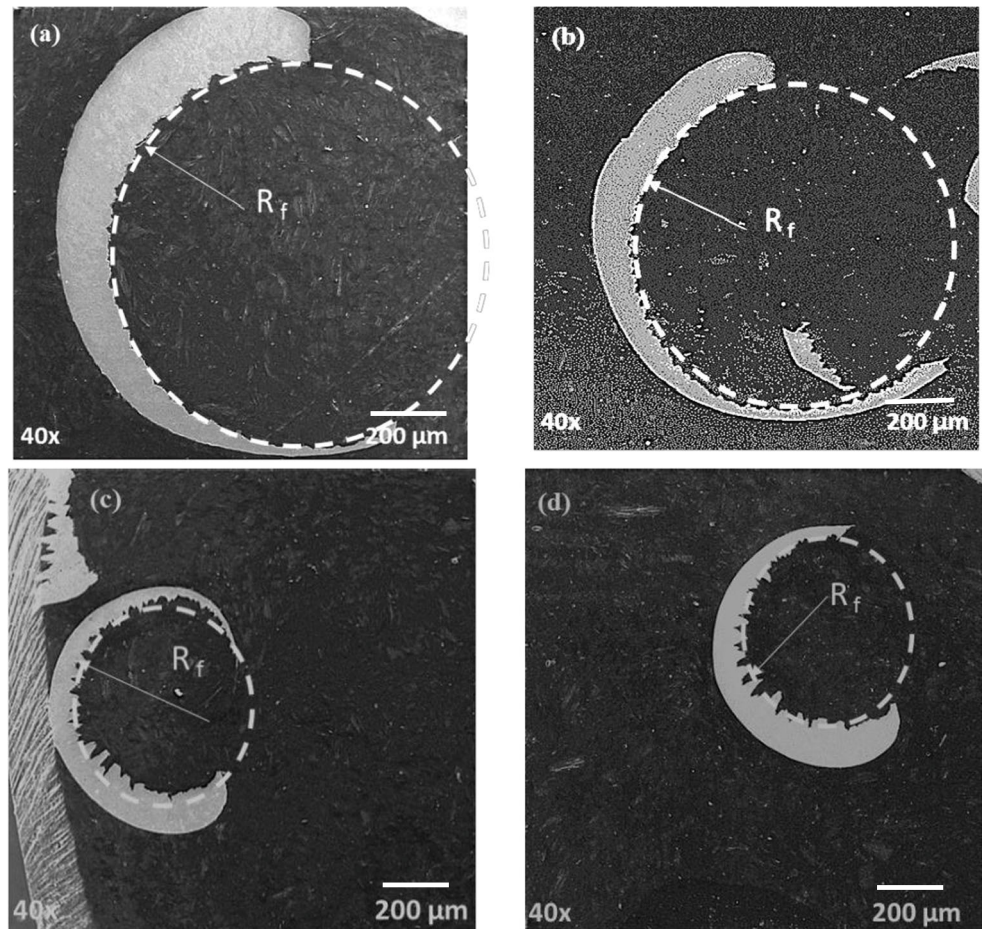
behavior still merits further investigation, which may help to develop a more effective system with favorable chip breaking properties.

## 5.2 Model assumptions

The machining operation is a sophisticated process; thus, several assumptions were made to predict the chip upcurl radius. The theoretical model thus assumes the following holds true:

(1) Tool edge radius is neglected
(2) Chip formation is continuous
(3) Volume is constant
(4) There is no material separation
(5) The chip forming after the application of HPC has no further plastic deformation
(6) The cutting tool and the machining system are rigid during the cutting operation

**Fig. 14** **a** Graphical representation of shear plane model. **b** Deformation axes for chip curling phase [42]
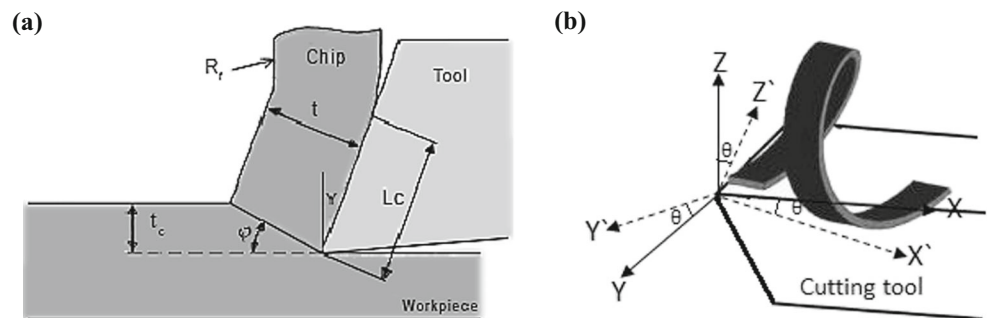
## 5.3 Derivation based on shear plane theory

As discussed in the previous section, the chip plastic strain ($\varepsilon_{up}$) is a function of both $t_c$ and $R_f$ (Fig. 14a). $\varepsilon_{up}$ is proportional to $t_c$ and inversely proportional to $R_f$ (Eq. 5). To predict the value of $R_f$, it is necessary to predict the values of $\varepsilon_{up}$ and $t_c$. $t_c$ can be calculated from Eq. 6.

$$t_c = \frac{t}{r} \tag{6}$$

where thickness ratio, $r$, is assumed to be 0.05. Thus, $t_c$ can be assumed to be 0.05 t. $t$ can also be calculated from Eq. 7.

$$t = f \cos\Phi \tag{7}$$

To be able to define the tensor of the chip strain, the tensor is conducted around the rotation angle ($\theta$) (Fig. 14b). This tensor can be described using Mohr's circle relationship. Equation 8 relates the transformation of a strain tensor from the unrotated ab-coordinate system. Here, the tensor is assumed to be rotated around the third axis ($\psi$).

$$\varepsilon_{up} = \begin{vmatrix} \varepsilon_a & \gamma_{ab} \\ \gamma_{ba} & \varepsilon_b \end{vmatrix} \tag{8}$$

Considering the deformation axes and volume constancy, $\varepsilon_a$, $\varepsilon_b$, and $\gamma_{ab} = \gamma_{ba}$ can be calculated as follows:

$$\varepsilon_a = \frac{\varepsilon_{ax} + \varepsilon_{ay}}{2} \tag{9}$$

$$\varepsilon_b = \frac{\varepsilon_{bx} + \varepsilon_{by}}{2} \tag{10}$$

$$\varepsilon_a = \frac{\varepsilon_x + \varepsilon_z}{2} + \frac{\varepsilon_x - \varepsilon_z}{2} \cos(2\psi) \tag{11}$$

$$\varepsilon_b = \frac{\varepsilon_a + \varepsilon_b}{2} - \frac{\varepsilon_a - \varepsilon_b}{2} \cos(2\psi) \tag{12}$$

$$\gamma_{dc} = \frac{-\varepsilon_a - \varepsilon_b}{2} \sin(2\psi) \tag{13}$$

By using Mohr's circle relationship, $\varepsilon_{ax}$, $\varepsilon_{bx}$, $\varepsilon_{ay}$, $\varepsilon_{by}$, and $R$ can be calculated as follows:

$$\varepsilon_{ax} = \frac{\varepsilon_{xx} + \varepsilon_{zx}}{2} + \frac{\varepsilon_{xx} - \varepsilon_{zx}}{2} \cos(2\psi) + \gamma_{xz}\sin(2\psi) \tag{14}$$

$$\varepsilon_{ay} = \frac{\varepsilon_{xy} + \varepsilon_{zy}}{2} + \frac{\varepsilon_{xy} - \varepsilon_{zy}}{2} \cos(2\psi) - \gamma_{xz}\sin(2\psi) \tag{15}$$

$$\varepsilon_{bx} = \frac{\varepsilon_{xx} + \varepsilon_{zx}}{2} + \frac{\varepsilon_{xx} - \varepsilon_{zx}}{2} \cos(2\psi) + \gamma_{xz}\sin(2\psi) \tag{16}$$

$$\varepsilon_{by} = \frac{\varepsilon_{xy} + \varepsilon_{zy}}{2} + \frac{\varepsilon_{xy} - \varepsilon_{zy}}{2} \cos(2\psi) - \gamma_{xz}\sin(2\psi) \tag{17}$$

$$R = \frac{-\varepsilon_a - \varepsilon_b}{2} \sin(2\psi) + \gamma_{ab}\cos(2\psi) \tag{18}$$

According to that, the chip upcurl strain tensor can be expressed in the XYZ coordinate system as follows:

$$\varepsilon_{up} = \begin{vmatrix} \frac{\varepsilon_x + \varepsilon_z}{2} + \frac{\varepsilon_x - \varepsilon_z}{2}\cos(2\psi) + \gamma_{ab}\sin(2\psi) & 0 & \frac{-\varepsilon_x - \varepsilon_z}{2}\sin(2\psi) + \gamma_{ab}\cos(2\psi) \\ 0 & \varepsilon_y = \varepsilon_z & 0 \\ \frac{-\varepsilon_x - \varepsilon_z}{2}\sin(2\psi) + \gamma_{ab}\cos(2\psi) & 0 & \frac{\varepsilon_x + \varepsilon_z}{2} - \frac{\varepsilon_x - \varepsilon_z}{2}\cos(2\psi) - \gamma_{ab}\sin(2\psi) \end{vmatrix} \tag{19}$$

To solve the tensor, $I_1$, $I_2$, and $I_3$ should be calculated as follows:

$$-\varepsilon^3 + I_1\varepsilon^2 - I_2\varepsilon + I_3 = 0 \tag{20}$$

$$I_1 = \varepsilon_x + \varepsilon_y + \varepsilon_z \tag{21}$$

$$I_2 = \varepsilon_x\varepsilon_y + \varepsilon_y\varepsilon_z + \varepsilon_x\varepsilon_z - \gamma_{xy}^2 - \gamma_{xz}^2 - \gamma_{yz}^2 \tag{22}$$

$$I_3 = \varepsilon_x\varepsilon_y\varepsilon_z + 2\varepsilon_{xy}\varepsilon_{xz}\varepsilon_{yz} - \varepsilon_{xy}^2\varepsilon_z - \varepsilon_{xz}^2\varepsilon_y - \varepsilon_{yz}^2\varepsilon_{zx} \tag{23}$$

By knowing the values of $I_1$, $I_2$, and $I_3$, $\varepsilon_{up}$ can be obtained from Eq. 19 and $R_f$ from Eq. 5.

## 5.4 Derivation based on structural mechanics theory

HPC used with continuous chip production may strike the chip, creating a reactive force on it, causing a bending moment to act along the chip body, which in turn, bends the chip [46]. In this case, the curved chip can be considered to be a statically determinant curved beam as shown in Fig. 15a. To analyze the force system on the curled chip, the chip may be regarded as a free body held in static equilibrium and the force system acting on it (Fig. 15b) [47].

$$R_1 + R_2 + R_3 = 0 \tag{24}$$

By using the vector equilibrium relationship of forces (Eq. 24), the equation can be expressed as follows:

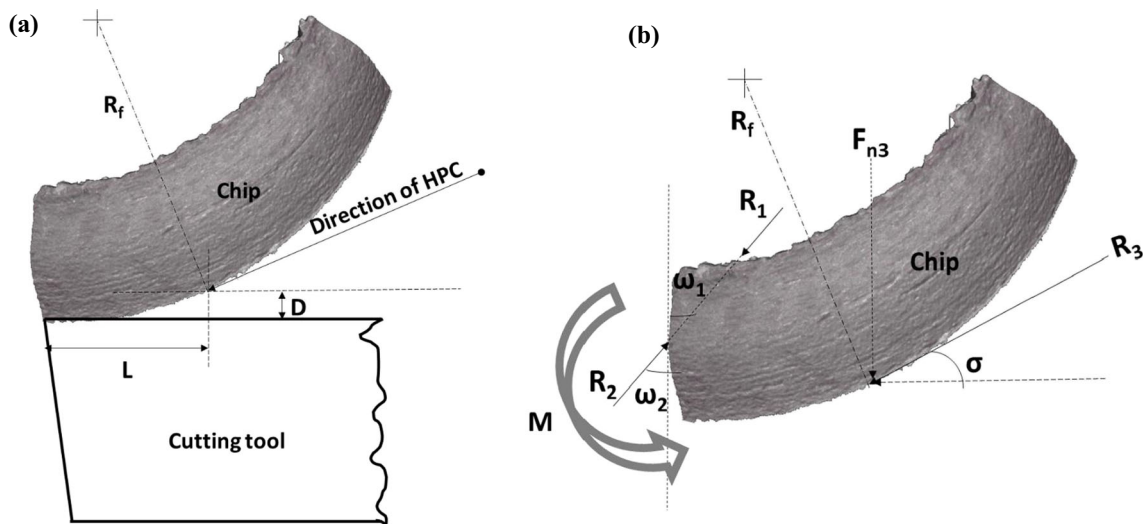$$-R_1 \sin\omega_1 + R_2 \sin\omega_2 + F_{n3}\cos\sigma + F_3\cos(90 - \sigma) = 0 \tag{25}$$

**Fig. 15** **a** The force model for HPC, hitting chip. **b** The free body diagram of chip curling

$$R_1 cos\omega_1 - R_2 cos\omega_2 - F_{n3} Sin\sigma - F_3 sin(90 - \sigma) = 0 \tag{26}$$

The friction force ($F_3$) can be expressed as $F_3 = \mu F_{n3}$, where $\mu$ is the friction coefficient; thus, $\mu$ can be expressed by

$$\mu = \frac{F_3}{F_{n3}} \tag{27}$$

From Eqs. 25, 26, and 27, $R_2$ can be expressed as follows:

$$R_2 = \frac{F_{n3}}{sin\omega_2} \tag{28}$$

Substitution of Eq. 27 into Eq. 28, $F_3$ and $F_{n3}$ can be expressed as follows:

$$F_{n3} = \frac{R_1(cos\omega_1 sin\omega_2 - cos\omega_2 sin\omega_1)}{cos\omega_2 Cos\sigma - sin\omega_2 Sin\sigma + \mu(sin\omega_2 cos\sigma + cos\omega_2 Sin\sigma)} \tag{29}$$

$$F_3 = \frac{\mu R_1(cos\omega_1 sin\omega_2 - cos\omega_2 sin\omega_1)}{cos\omega_2 Cos\sigma - sin\omega_2 Sin\sigma + \mu(sin\omega_2 cos\sigma + cos\omega_2 Sin\sigma)} \tag{30}$$

The bending moment which results from HPC can be obtained, based on the force equilibrium principle, from the following:

$$M = F_3 R_f(1 - Cos\delta) - F_{n3} R_f Sin\delta \tag{31}$$

Or,

$$M = F_{n3} R_f(\mu - \mu Cos\delta - Sin\delta). \tag{32}$$

From the values of $F_{n3}$, $M$, $\mu$, and spiral angle ($\theta$), final chip upcurl radius can be calculated:

$$R_f = \frac{M}{F_{n3}(\mu - \mu cos\delta - sin\delta)} \tag{33}$$

From Eqs. 5, 19, and 33, the final chip upcurl radius obtained by HPC is

$$R_{fHPC} = \left| \frac{t_c}{2\varepsilon_{up}} - \frac{M}{F_{n3}(\mu - \mu cos\delta - sin\delta)} \right| \tag{34}$$

where $t_c$, $\varepsilon_{up}$, and $\mu$, $F_{n3}$, $M$ are determined by Eqs. 5, 19, 27, 29, and 32, respectively.

## 5.5 Model validation

The theoretical model established above to predict the resultant chip upcurl radius was evaluated for its credibility. The experimental values of chip upcurl radius were compared to the predicted values obtained from the theoretical models (Fig. 16). Figure 16a, b shows the average prediction errors at different feed rates for HPC (35 bar) and HPC (70 bar), respectively. As shown, the resultant chip upcurl radius values generated by the model gave results very close to the experimental values of the resultant chip upcurl radius with an error of 5–6%.

In addition, in Fig. 16c, d, the average prediction errors at different cutting speeds are 8% and 9% for HPC (35 bar) and HPC (70 bar), respectively. This indicates that the proposed model is reliably able to predict the chip upcurl radius even at different cutting speeds. From these comparisons, it can be concluded that the theoretical model can make a very good
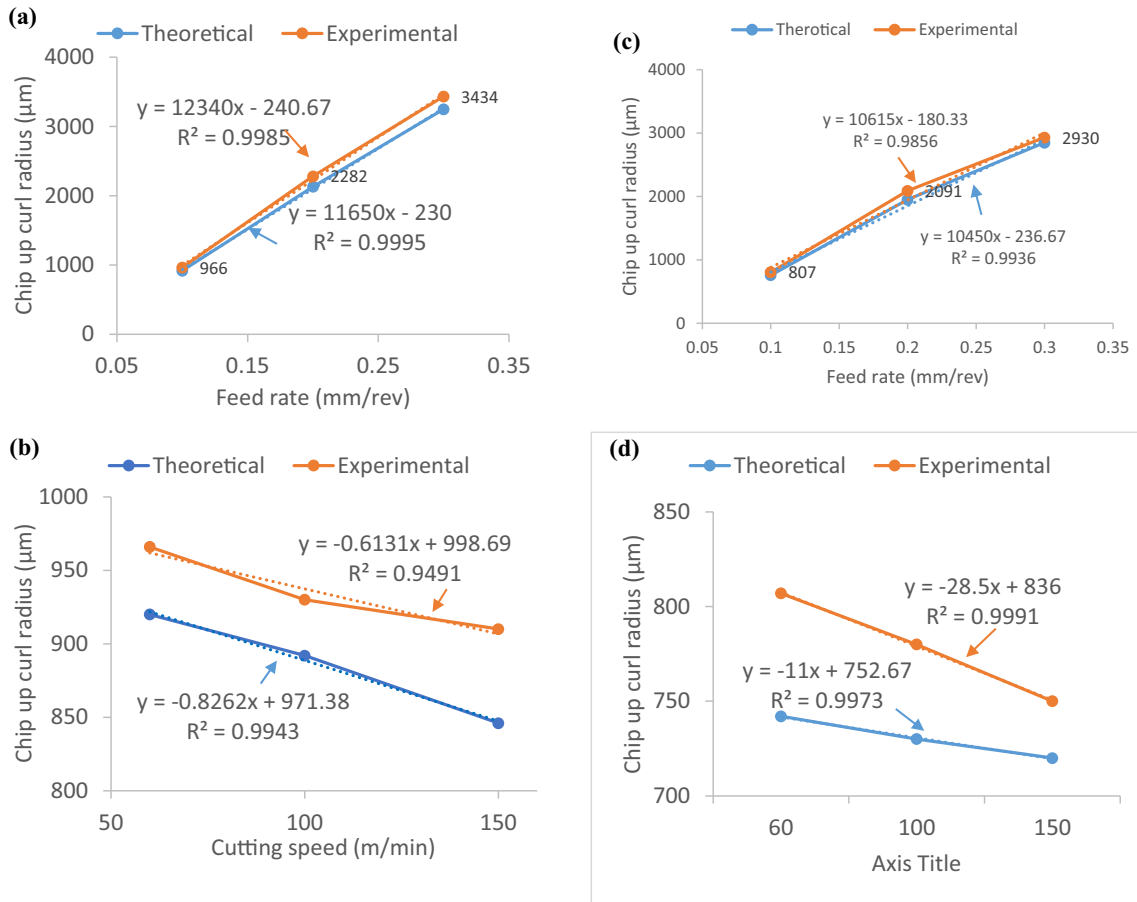
**Fig. 16** Comparison between the average values of theoretical and experimental chip curl radius with **a**, **b** HPC of 35 bar and **c**, **d** HPC of 70 bar

**Table 4**    Validation of experiment

| HPC | Cutting speed (m/min) | Feed rate (mm/rev) | Average experimental value (μm) | Average theoretical value (μm) | Error (%) |
|---|---|---|---|---|---|
| 35 bar | 60 | 0.1 | 920 | 966 | 5 |
| | | 0.2 | 2130 | 2282 | 7 |
| | | 0.3 | 3250 | 3434 | 5.6 |
| | 100 | 0.1 | 950 | 912 | 4 |
| | | 0.2 | 2250 | 2115 | 6 |
| | | 0.3 | 3122 | 2915 | 6.6 |
| | 150 | 0.1 | 910 | 846 | 7 |
| | | 0.2 | 2232 | 2101 | 5.9 |
| | | 0.3 | 3015 | 2880 | 4.5 |
| 70 bar | 60 | 0.1 | 807 | 742 | 8 |
| | | 0.2 | 2091 | 1950 | 6.7 |
| | | 0.3 | 2930 | 2850 | 2.7 |
| | 100 | 0.1 | 790 | 740 | 2 |
| | | 0.2 | 1998 | 1820 | 6.3 |
| | | 0.3 | 2710 | 2513 | 7.2 |
| | 150 | 0.1 | 720 | 665 | 7.6 |
| | | 0.2 | 1807 | 1730 | 4.2 |
| | | 0.3 | 2520 | 2320 | 7.9 |

prediction for the chip upcurl radius at different HPC conditions as well as at different cutting conditions.

Table 4 shows the exact percentage of error between the results obtained from experimental and theoretical model values for the two different HPC conditions at different cutting conditions. This shows that the theoretical model can be used in the future to monitor chip breakability under HPC supply at different cutting conditions.

# 6 Conclusions

In this research, multiple experiments were conducted to investigate the chip morphology and the chip forming mechanism during machining of AISI 304 stainless steel with an HPC system, and to compare the results with those of dry and conventional coolant. From the experimental results and theoretical model, the specific conclusions can be drawn:

1)  HPC conditions help to break up chips, producing shorter segmented chips, which in turn enhance the process efficiency. However, dry and conventional coolant did not show a distinct effect on chip breakability.
2)  HPC conditions produce more regular serration in the chips, compared with absent segmentation observed in dry and conventional coolant.
3)  Tribological performance was improved with HPC. Lower chip thickness and higher shear angle are obtained under HPC conditions, compared to dry and conventional coolant, which in turn leads to a decrease in cutting forces, and increase in chip curl to improve chip control.
4)  The chip undersurface is smooth and has no observable defects under HPC conditions, indicating low tool-chip contact length and consequently lower friction between the chip and the cutting tool.
5)  The variation of flank wear affects the chip forming mechanism and its segmentation. Machining with new tool inserts under dry and conventional coolant, generated continuous chips, and upon increasing flank wear, the type of generated chip transitions from continuous to saw-tooth. This is due to high friction between the worn cutting edge and chip, leading to significant shear on the machined surface in the chip.
6)  No significant difference was found in the degree of segmentation in the case of HPC at different flank wears, which indicates that the flank wear did not affect the chip segmentation whenever HPC is used. This is due to severe plastic deformation caused by HPC application.
7)  Lastly, a 3D theoretical model was developed to predict the chip upcurl radius under HPC machining and the

results were found to be in good agreement with actual measurements taken from a machining experiment with AISI 304 stainless steel.

**Publisher's note** Springer Nature remains neutral with regard to jurisdictional claims in published maps and institutional affiliations.

## References

1.  Xavior MA (2012) Evaluating the machinability of AISI 304 stainless steel using alumina inserts. J Achiev Mater Manuf Eng 55:841–847
2.  Gariani S, Shyha I, Inam F, Huo D (2017) Evaluation of a novel controlled cutting fluid impinging supply system when machining titanium alloys. Appl Sc 7:560
3.  Rahman M, Senthil Kumar A, Choudhury MR (2000) Identification of effective zones for high pressure coolant in milling. CIRP Ann Manuf Technol 49:47–52
4.  Mia M, Dhar NR (2018) Effects of duplex jets high-pressure coolant on machining temperature and machinability of Ti-6Al-4V superalloy. J Mater Process Technol 252:688–696
5.  Liu E, Han R, Tan G, Li Z (2006) Analysis of chip breaking prediction in cutting aluminum alloys. Mater Sci Forum 532:213–216
6.  Kaminski J, Alvelid B (2000) Temperature reduction in the cutting zone in water-jet assisted turning. J Mater Process Technol 106:68–73
7.  Kubala Z (1989) Metal machining with high- pressure water-jet cooling assistance—a new possibility. J Eng Ind 111:7–12
8.  Courbon C, Sajn V, Kramar D, Rech J, Kosel F, Kopac J (2011) Investigation of machining performance in high pressure jet assisted turning of Inconel 718: an experimental study. J Mater Process Technol 211:1834–1851
9.  Palanisamy S, Townsend D, Scherrer M, Andrews R, Dargusch MS (2009) High pressure coolant application in milling titanium. Mater Sci Forum 618:89–92
10.  Machado AR, Wallbank J, Pashby IR, Ezugwu EO (1998) Tool performance and chip control when machining Ti6A14V and inconel 901 using high pressure coolant supply. Mach Sci Technol 2:1–12
11.  Guidance UT (2005) An analysis of strain in chip breaking using slip-line field theory with adhesion friction at chip / tool. J Mater Process Technol 170(1):509–515
12.  Joshi SS, Ramakrishnan N, Ramakrishnan P (1999) Analysis of chip breaking during orthogonal machining of Al/SiCp composites. J Mater Process Technol 88(1):90–96
13.  Henriksen Ek (1954) Chip breaker dtudies I: design and performance of ground chip breakers, Engineering Reprint Series Reprint Number 12 The University of Missouri Bulletin, Missouri
14.  Okushima K, Minato K (1959) On the behaviour of chip in steel cutting. Bulletin JSME 2(5):58–64
15.  Sandvik Coromant (2017) Turning tools, Switzerland
16.  Koyee RD, Schmauder S, Heisel U, Eisseler R (2015) Numerical modeling and optimization of machining duplex stainless steels. Prod Manuf Res 3:36–83
17.  Panda A, Duplák J, Vasilko K (2012) Analysis of cutting tools durability compared with standard ISO 3685. Int J Comput Theory Eng 4(4):621–624

18. Shaw M (2005) Metal cutting principles, 2nd edn. Oxford Unversity Press, New York

19. ISO (2000) ISO 5436-1:2000 (en): Geometrical product specifications (GPS)—surface texture: profile method, Measurement standards–part1, Geneva, Switzerland

20. Shivpuri R, Hua J, Mittal P, Srivastava AK, Lahoti GD (2002) Microstructure-mechanics interactions in modeling chip segmentation during titanium machining. CIRP Ann 51(1):71–74

21. Mia M, Dhar NR (2015) Effect of high pressure coolant jet on cutting temperature, tool wear and surface finish in turning hardened (Hrc 48) steel. J Mech Eng 45(1):1–16

22. Abukhshim NA, Mativenga PT, Sheikh MA (2004) An investigation of the tool-chip contact length and wear in high-speed turning of EN19 steel. Proc Inst Mech Eng B J Eng Manuf 218(8):889–903

23. Wan ZP, Zhu YE, Liu HW, Tang Y (2012) Microstructure evolution of adiabatic shear bands and mechanisms of saw-tooth chip formation in machining Ti6Al4V. Mater Sci Eng A 531(1):155–163

24. Habak M, Lou Lebrun J (2011) An experimental study of the effect of high-pressure water jet assisted turning (HPWJAT) on the surface integrity. Int J Mach Tools Manuf 51(9):661–669

25. Haddag B, Makich H, Nouari M, Dhers J (2015) Characterization and modelling of the rough turning process of large-scale parts: tribological behavior and tool wear analyses. Procedia CIRP 31(1):293–298

26. Bi XF, Sutter G, List G, Liu YX (2009) Influence of chip curl on tool-chip contact length in high speed machining. Mater Sci Forum 626(1):71–74

27. Molinari A, Musquar C, Sutter G (2002) Adiabatic shear banding in high speed machining of Ti-6Al-4V: experiments and modeling. Int J Plast 18(1):443–459

28. Miguèlez MH, Soldani X, Molinari A (2013) Analysis of adiabatic shear banding in orthogonal cutting of Ti alloy. Int J Mech Sci 75(1):212–222

29. Barry J, Byrne G (2002) The mechanisms of chip formation in machining hardened steels. J Manuf Sci Eng 124(3):528–545

30. Sima M, Özel T (2010) Modified material constitutive models for serrated chip formation simulations and experimental validation in machining of titanium alloy Ti-6Al-4V. Int J Mach Tools Manuf 50(11):943–960

31. Da Silva RB, MacHado AR, Ezugwu EO, Bonney J, Sales WF (2013) Tool life and wear mechanisms in high speed machining of Ti-6Al-4V alloy with PCD tools under various coolant pressures. J Mater Process Technol 213(8):1459–1464

32. Gajrani KK, Sankar MR (2017) ScienceDirect state of the art on micro to nano textured cutting tools. Mater Today Proc 4(2):3776–3785

33. Khan MA (2015) Effect of high pressure coolant jets in turning Ti-6al-4v alloy with specialized designed nozzle. Dissertation, Bangladesh University of Engineering & Technology Dhaka

34. Jawahir IS (1990) On the controllability of chip breaking cycles and modes of chip breaking in metal machining. CIRP Ann Manuf Technol 39(1):47–51

35. Wang B, Liu Z (2016) Evaluation on fracture locus of serrated chip generation with stress triaxiality in high speed machining of Ti6Al4V. Mater Des 98(1):68–78

36. Skrzypek J, Ganczarski A (1999) Modeling of material damage and failure of structures. Theory and Applications, London

37. Nakayama K, Arai M, Kanda T (2011) Machining characteristics of hard materials. Mach Hard Mater 37(1):1–21

38. Zhou L (2011) Machining chip-breaking prediction with grooved inserts in steel turning, dissertation, Worcester Polytechnic Institute

39. Buchkremer S, Schoop J (2016) A mechanics-based predictive model for chip breaking in metal machining and its validation. CIRP Ann Manuf Technol 65(1):69–72

40. Devotta A, Beno T, Löf R, Espes E (2015) Quantitative characterization of chip morphology using computed tomography in orthogonal turning process. Procedia CIRP 33(1):299–304

41. Merchant ME (1945) Mechanics of the metal cutting process. II. Plasticity conditions in orthogonal cutting. J Appl Phys 16(1):318–324

42. Astakhov VP, Shvets SV, Osman MOM (1997) Chip structure classification based on mechanics of its formation. J Mater Process Technol 71(2):247–257

43. Buchkremer S, Klocke F, Lung D (2015) Finite-element-analysis of the relationship between chip geometry and stress triaxiality distribution in the chip breakage location of metal cutting operations. Simul Model Pract Theory 55(1):10–26

44. Buchkremer S, Klocke F, Lung D (2014) Analytical study on the relationship between chip geometry and equivalent strain distribution on the free surface of chips in metal cutting. Int J Mech Sci 85:88–103

45. Nomani J, Pramanik A, Hilditch T, Littlefair G (2017) Stagnation zone during the turning of Duplex SAF 2205 stainless steels alloy. Mater Manuf Process 32(13):1486–1489

46. Klocke F, Sangermann H, Krämer A, Lung D (2011) Influence of a high-pressure lubricoolant supply on thermo-mechanical tool load and tool wear behavior in the turning of aerospace materials. Proc Inst Mech Eng B J Eng Manuf 225(1):52–61

47. Çolak O (2012) Investigation on machining performance of Inconel 718 under high pressure cooling conditions. Stroj Vestn-J Mech Eng 58(11):683–690

48. Kamruzzaman M, Dhar NR (2008) The effect of applying high-pressure coolant (HPC) jet in machining of 42crmo4 steel by uncoated carbide inserts. J Mech Eng 39(2):71–77

49. Ezugwu EO, Bonney J (2004) Effect of high-pressure coolant supply when machining nickel-base, Inconel 718, alloy with coated carbide tools. J Mater Process Technol 153(1):1045–1050

50. Zhou L, Rong Y, Li Z, Yang JA (2003) Development of web-based machining chip breaking prediction systems. Int J Adv Manuf Technol 22(5):336–343

51. Zhang YZ, Peklenik J (1980) Chip curl, chip breaking and chip control of the difficult-to-cut materials. CIRP Ann Manuf Technol 29(1):79–83